Draft version December 11, 2017
Typeset using LaTeX **twocolumn** style in AASTeX61

THE ISOTHERMAL OUTFLOW IN THE HIGH-MASS STAR-FORMING REGION G240.31+0.07

Junhao Liu[1] and Keping Qiu[1]

[1] *School of Astronomy & Space Science, Nanjing University, Nanjing, P.R.China*

ABSTRACT

We present Atacama Pathfinder Experiment (APEX) observations toward the massive star-forming region G240.31+0.07 in the CO (3-2), (6-5), and (7-6) lines. The integrated high-velocity and low-velocity emissions of the three lines reveal a bipolar outflow and show similarity in morphology. Using the three CO lines, together with the combined data from the Submillimeter Array (SMA) and the Caltech Submillimeter Observatory (CSO) 10.4 m telescope in CO (2-1), we estimate the physical parameters of the G240.31+0.07 outflow as a function of gas velocity, by the means of large velocity gradient (LVG) modeling and rotalation diagram (RD) analysis. Our results reveal that the temperature of the outflow has an almost constant value of ~ 50 K, which is consistent with the isothermal assumption of the wide-angle wind-driven model. We also find a decreasing trend of CO column density with gas velocity. In addition, the modeling results reveal that the outflowing gas is thermalized and no upper limits to the gas density could be derived. The lower limits of gas density are $n_{\rm low} \sim 10^5$ cm^{-3}. We also detect a decreasing gas density with velocity if we assume a constant CO abundance ratio and a constant velocity gradient.

Keywords: ISM: individual objects(G240.31+0.07) - ISM: jets and outflows - stars: formation

Corresponding author: Keping Qiu
kpqiu@nju.edu.cn

1. INTRODUCTION

Bipolar molecular outflows, mostly observed via CO and HCO^+ and their isotopes, are a common phenomenon associated with young stellar objects (YSOs) of all masses(Lada 1985; Fukui et al. 1993; Zhang et al. 2001; Beuther et al. 2002; Wu et al. 2004, 2005; Ferreira et al. 2006; Arce et al. 2007; Maud et al. 2015). In sites of low-mass star formation, molecular outflows involve amounts of energy similar to those involved in the accretion processes and are indispensable for dissipating excess angular momentum of accretion disks (Shu et al. 1987; Bachiller 1996). Given the fact that outflows can continuously inject momentum into supersonic turbulence to keep the cloud from collapsing, outflows are essential to explain the low star formation efficiency in turbulent clouds. outflows also play a key role in determining the core-to-star efficiencies (Frank et al. 2014). Thus, molecular outflows are a fundamental part of the formation process of low mass stars.

The dirving mechanism of molecular outflows remains unknown. Traditionally, molecular outflows from low-mass protostars were thought to be entrained by a wide-angle wind (Shu et al. 1991; Lee et al. 2001), or by a jet bow shock (Raga & Cabrit 1993; Masson & Chernin 1993; Lee et al. 2001). In the wind-driven model, a molecular outflow is the ambient material swept-up by a wide-angle radial wind. In the jet-driven model, a molecular outflow is accelarated by a jet bow shock when a jet propagates into the ambient gas. Though these models predict many different outflow properties (Arce et al. 2007), most of the previous observational work has focused on comparing the morphology and the kinematics of outflows with the model predictions. The shapes of molecular outflows range from parabolic molecular shells in RNO 91 and VLA 05487 (Lee et al. 2000), which is consistent with the wind-driven model, to the bow-shaped shells in HH211 (Gueth & Guilloteau 1999) and HH 212 (Lee et al. 2000, 2015), which is consistent with the jet-driven model. There are also outflows where the two diffferent features exist simultaneously (HH 111, Lee et al. (2000); HH 46/47, Arce et al. (2013), Zhang et al. (2016); IRAS 04166+2706, Santiago-García et al. (2009)). Between the wind-driven model and the jet-driven model, their predictions on the P-V diagrams cut along the outflow axis can be clearly distinguished: a convex spur structure with the highest velocity at the bow tip as predicted by the jet-driven model and a parabolic structure originating from the central source as predicted by the wind-driven model (Lee et al. 2001). The P-V relations of some CO outflows are best explained by the jet-driven model, such as the outflows of HH 212 and HH 240/241 (Lee et al. 2000). And the P-V relations of some other CO outflows are best explained by the wind-driven model, such as the outflows drived by IRAS 16293-2422 (Yeh et al. 2008) and VLA 05847+0255 (Lee et al. 2000). On the other hand, the P-V structure of some CO outflows need to be explained by a combination of a jet-driven model and a wind-driven model, such as the HH 111 outflow (Lee et al. 2000) and the HH 46/47 outflow (Arce et al. 2013). The wind-driven model and the jet-driven model also show a difference between the power-law index of the M-V relation. However, different simulations of each model have yielded different slopes for the computed CO intensity-velocity relations, making it difficult to compare the observed power-law index with the model predictions. For a outflow drived by a low-mass YSO, the wind-driven models generally predict a smaller intensity-velocity power-law index over a narrower range when compared to the jet-driven models (Arce et al. 2007).

Though the wind-driven model and the jet-driven model can each explain the characteristics of some observed outflows, none of them are capable of producing the observed features of all types of outflows (Lee et al. 2002). To explain the two types of outflows simultaneously, two-component models with both highly collimated jet and wide-angle wind have been developed (Banerjee & Pudritz 2006; Pudritz et al. 2006; Shang et al. 2006; Pudritz et al. 2007; Machida et al. 2008; Machida 2017).

Due to the rarity and typically larger distances, the case of massive molecular outflows is more problemtic than their low-mass counterparts. And there is little work on modeling outflows from high-mass YSOs. Observations have shown that the masses, momenta and energy of molecular outflows from massive YSOs are higher than their low-mass counterparts (Beuther et al. 2002; Wu et al. 2005), and the morphology and kinematics of some outflows driven by massive YSOs are very similar to the outflows driven by low mass YSOs (Shepherd et al. 1998; Beuther et al. 2002; Caratti o Garatti et al. 2008; Qiu et al. 2009; Ren et al. 2011; Su et al. 2012). Many questions, e.g., how the outflows from massive YSOs are accelerated, how they differ from low-mass outflows, and how they affect the high-mass star-forming processes, are still unanswered. It is essential to address these questions by studying individual outflows associated with high-mass star-forming regions.

Most previous studies of outflows have used low-J rotational transitions of CO (transitions up to $J_u = 4$, with upper-state energies $E_u < 50$ K), which are easily excited at low temperatures, to characterize the relatively cold and extended molecular gas in morphology

and kinematics (Shepherd et al. 1998; Su et al. 2004; Yeh et al. 2008; Qiu et al. 2009; Santiago-García et al. 2009; Arce et al. 2013; Zhang et al. 2016). These low-J CO emission lines can be easily observed from the ground-based facilities. Due to atmospheric limits, observations of mid-J CO lines (referring to CO (6-5) and CO (7-6) throughout this paper), which are less affected by ambient gas and can probe the warm and/or dense gas, are very rare. To derive the physical parameters of the outflowing gas, sensitive observations of CO across multiple transitions are needed.

This paper is a follow-up study of the G240.31+0.07 (hereafter G240) outflow (Qiu et al. 2009). Here we report the 12-m submillimeter Atacama Pathfinder Experiment Telescope[1] (APEX) observations of G240, an active high-mass star-forming region which is associated with the young stellar object (YSO) IRAS 07427-2400 and located at a distance of 5.41 kpc (Sakai et al. 2015). It harbors an ultracompact HII region and is associated with OH and H_2O masers (Hughes & MacLeod 1993; Caswell 1997; MacLeod et al. 1998; Migenes et al. 1999; Caswell 2003). Its far-infrared luminosity of $10^{4.7}$ $L_\odot$ is consistent with a spectral type O8.5 zero-age main-sequence star (MacLeod et al. 1998). A near-infrared study has found two bright elongated H_2 emission knots near the source (Kumar et al. 2002). Kumar et al. (2003) further argued that the shocked H_2 emission indicates the presence of a massive rotating disk/envelope around the luminous YSO IRAS 07427-2400.

There are also millimeter and centimeter radio continuum observations toward G240. Two clumps were detected by Chen et al. (2007) at 654 GHz (460 μm), with clump A coinciding with a VLA 6 cm point source (Hughes & MacLeod 1993) and an H_2O maser. Qiu et al. (2009) presented a high resolution interferometric study at 1.3 mm and resolved the central part of G240 into three dusty cores MM1, MM2, and MM3, with the brightest core MM1 coinciding with the VLA 6 cm point source spatially. Trinidad (2011) presented observations at 1.3, 3.6, and 6 cm and reported radio continuum emissions at the position of the three millimeter sources in at least one wavelength.

G240 has also been mapped with single dish and interferometric observations in CO emission. High-velocity CO (1-0) gas was detected towards G240 (McCutcheon et al. 1991; Shepherd & Churchwell 1996), tracing a bipolar outflow (Shepherd & Churchwell 1996). Hunter (1997) mapped the CO (3-2) emission with a 20″ beam and found a prominent bipolar outflow at a position angle (PA) of 138° and a weaker component at PA ∼ 101°. Kumar et al. (2003) also detected a prominent component and a weaker component of the bipolar CO (3-2) outflow with a 20″ beam and reported the PA of the prominent component to be 132°. Recently, Qiu et al. (2009) presented a detailed single dish and interferometric study of ^{12}CO (2-1) and ^{13}CO (2-1) emission and detected a bipolar, wide-angle, quasi-parabolic molecular outflow.

In addition, Qiu et al. (2014) reported the detection of an hourglass magnetic field aligned within 20° of the outflow axis.

In this paper, we present a CO multi-transition (3-2, 6-5, 7-6) study towards the G240 outflow. With large velocity gradient (LVG) calculations and rotation diagram (RD) analysis, we estimate the physical parameters of the outflow as a function of gas velocity. We then discuss the results of the analysis.

2. OBSERVATIONS

The APEX observations were conducted on . CO (6-5) and CO (7-6) were observed simultaneously. The pointing error of CO (6-5) and (7-6) was fixed by comparing them with the CO (2-1) data.

3. RESULTS

3.1. *CO EMISSIONS AND LINE RATIOS*

The cloud velocity (v_{cloud}) with respect to the local standard of rest is about 67.5 km s^{-1}, which is adopted from Kumar et al. (2003). Figure 1 shows the integrated low-velocity (LV) and high-velocity (HV) emissions of CO J = (2-1), (3-2), (6-5), (7-6). The outflow morphologies seen in CO (3-2), (6-5) and (7-6) are very similar. For the three lines detected by APEX, a prominent bipolar outflow at (PA) ∼ 131° along with a weaker component at PA ∼ 101° is detected. The weaker component is at relatively lower velocities, while the prominent component is detected at both low and high velocities. The signal-to-noise ratio in the CO (7-6) spectrum is relatively low at high velocities. Overall, the CO (3-2), (6-5), (7-6) maps presented in Figure 1 are very similar to the CO (3-2) map presented by Kumar et al. (2003). Due to angular resolution, the CO J = (3-2), (6-5), (7-6) emissions don't show the wide-angle structure highlighted by the CO (2-1) emission.

To compare the emissions of different CO transitions, we convolved the CO (2-1), (6-5) and (7-6) maps, to the same spatial resolution of the CO (3-2), which is 19″. To reduce the noise level in the spectra, we resampled the four CO lines to a resolution of 2 km s^{-1}. Then

[1] The Atacama Pathfinder Experiment Telescope is a collaboration between the Max-Planck-Institut für Radioastronomie, the European Southern Observatory, and the Onsala Space Observatory.

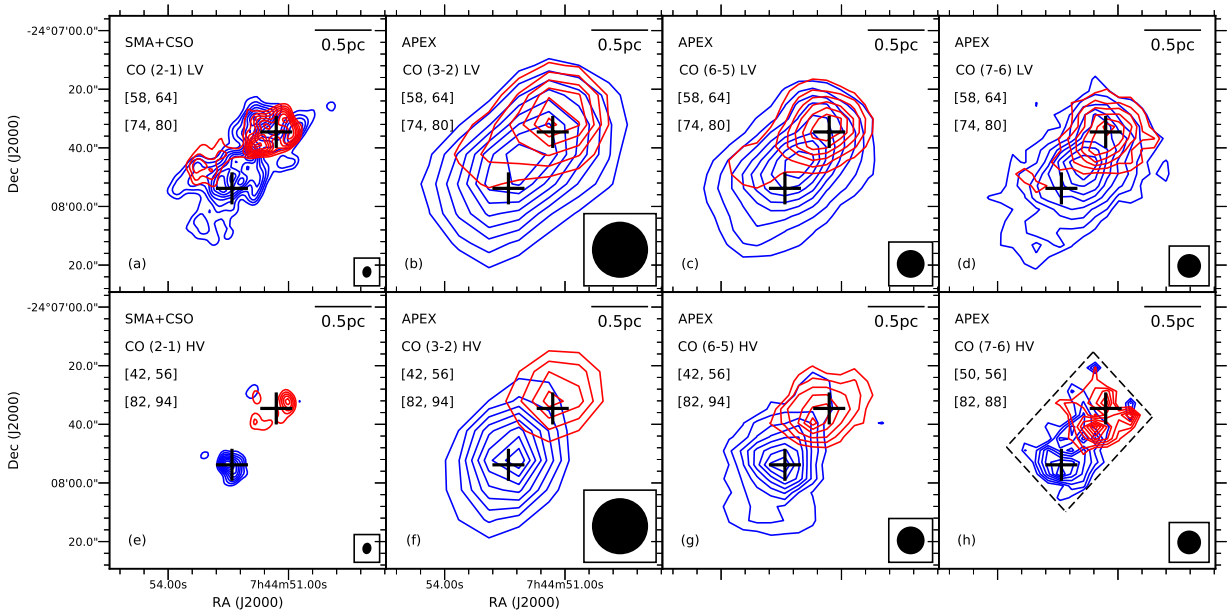

Figure 1. (a)-(d) Low-velocity CO J = (2-1), (3-2), (6-5), (7-6) emissions, integrated from 58 to 64 km s^{-1} for the blueshifted lobe (blue) and from 74 to 80 km s^{-1} for the redshifted lobe (red); (e)-(g) High-velocity CO J = (2-1), (3-2), (6-5) emissions, integrated from 42 to 56 km s^{-1} for the blueshifted lobe (blue) and from 82 to 94 km s^{-1} for the redshifted lobe (red); (h) High-velocity CO J = (7-6) emission, integrated from 50 to 56 km s^{-1} for the blueshifted lobe (blue) and from 82 to 88 km s^{-1} for the redshifted lobe (red). For (a)-(g), the contour levels start from 20% and continue at steps of 10% of the peak emission. For (h), the contour levels start from 30% and continue at steps of 10% of the peak emission. The beam size is shown in the lower right corner of each panel. The CO (2-1) maps are adopted from Qiu et al. (2009).

we measured the main beam temperature ($T_{\rm mb}$) of different CO lines at the peak of the blueshifted and the redshifted lobes (marked as two crosses in each panel of Figure 1). Figure 2 shows the observed line wing ratios of different CO transitions. All line ratios in Figure 2 are remarkably constant with velocity.

3.2. *PHYSICAL PROPERTY ANALYSIS*

Because the ^{13}CO emission is not detected in the outflowing gas, the four transitions of ^{12}CO are assumed to be optically thin during our analysis. Using the RADEX code (van der Tak et al. 2007), we construct a large grid of non-LTE models with three parameters: gas density ($n_{\rm H_2}$), kinetic temperature ($T_{\rm kin}$), and CO column density ($N_{\rm CO}$). Linewidths are given as input and are fixed to 2 km s^{-1}. The physical parameters in the outflow can be derived by comparing the main beam temperatures of various transitions with the model line intensities. Because of the degeneracies of the source size with the CO column density (in the optically thin case), all the computations are done with the assumption that the beam-filling factor is one for each transition. Thus, the derived physical parameters are the averaged values over the beam. The best fit is obtained by minimizing the

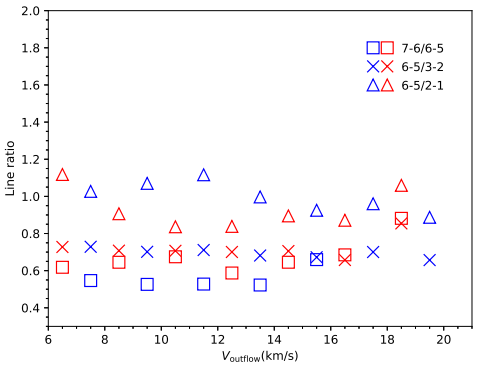

Figure 2. Ratios of the $T_{\rm mb}$ of different CO lines at different velocities. Blue symbols denote the measurements from the blueshifted lobe, and red symbols the redshifted lobe. The $V_{\rm outflow}$ shown here is related to the $v_{\rm cloud}$ by the relation: $V_{\rm outflow}$ = | $v_{\rm outflow}$ - $v_{\rm cloud}$ |, where $v_{\rm outflow}$ is the outflow velocity with respect to the local standard of rest.

χ^2 between the observed data and the model intensities. During the fitting, the intensity uncertainties of CO (2-1), CO (3-2), CO (6-5), CO (7-6) are set to 0.15, 0.2, 0.25, 0.3 respectively.

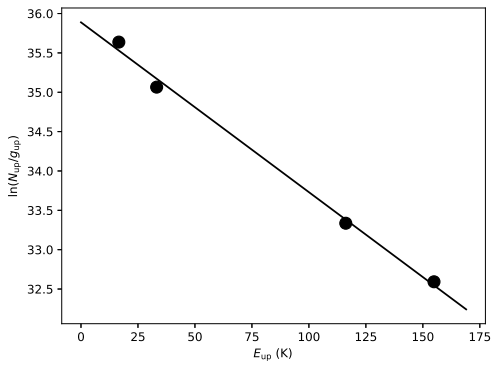

Figure 3. Rotation diagram for CO at 82 km s^{-1}. The fitted line shows the Boltzmann distribution of the rotational populations.

We also perform a rotation diagram (RD) analysis (Goldsmith & Langer 1999). Throughout the RD analysis, we assume that the outflow emission is optically thin and that the excitation of the sublevels is close to LTE. The population of each level is given by

$$N_{\rm up} = \frac{N_{\rm CO}}{Z} g_{\rm up} e^{-E_{\rm up}/kT_{\rm kin}}, \quad (1)$$

where $N_{\rm up}$ is the column density in the upper state, $g_{\rm up}$ the statistical weight of the upper state, $E_{\rm up}$ the upper energy level, k the Boltzmann constant, and Z is the partition function. RD for CO at 82 km s^{-1} as an example is shown in Figure 3. The molecular energy levels are in Boltzmann distribution. The RD behaves similarly at other velocities.

Figure 4 shows the outflowing gas temperature and the CO column density, estimated from the LVG analysiss and the RD analysis, as functions of gas velocity. The N-V diagram shows a clear decreasing trend of CO column density with outflow velocity, while the T-V diagram shows that the gas temperature has no obvious dependence on gas velocity. The χ^2 calculated from the LVG analysis are shown in the N-V diagram.

3.3. *THE ERROR OF THE FITTED PARAMETERS*

With four line observations and three simulation parameters, our fitting has one degree of freedom. Thus, the value of the reduced chi-square ($\chi^2_{\rm red}$) equals the value of the χ^2. As shown in Figure 4, the $\chi^2_{\rm red}$ of the best fitting results is less than 1 at most velocities, indicating that our adopted calibration error may be a bit conservative or the real value of degrees of freedom is smaller than one (Andrae et al. 2010). In Figure 5, we show cuts in the χ^2 along the [T, n], [T, N], [n, N] planes at 82 km s^{-1}, with all the other parameters fixed to the parameters of the best fitting result at this velocity, as examples of the χ^2 distribution. The χ^2 has only one minimum in [T, N] planes. However, the χ^2 distribution in the [T, n] and [n, N] planes show that the gas is thermalized and no upper limits to the density could be derived. The χ^2 distribution behaves similarly at other velocities.

The $\chi^2_{\rm red}$ of the best fitting results varies from 0.1 to 2.2 at different velocities. Considering the complexity of the data calibration process, the intensity uncertainty could vary with velocity. So the difference of the best-fitted $\chi^2_{\rm red}$ at different velocities could result from our adoption of a singularity intensity uncertainty of different transitions during the fitting. Though the best-fitted $\chi^2_{\rm red}$ have different values at different velocities,, the χ^2 distributions show similarity in morphology, indicating that the uncertainties of the fitted parameters may have similar level. So we derive the uncertainties of each parameter of the LVG analysis from the 1σ confidence region in the N-T-n 3-dimensional space at the velocities where $\chi^2_{\rm red} \sim 1$ as the representative uncertainties of the fitted parameters. The 1σ confidence range of temperature is about 40 K - 60 K. The lower limit of gas density ($n_{\rm lower}$) is around 10^5 cm^{-3}. The uncertainty of the CO column densitiy is $\sim$ 10 %.

We then perform the LVG analysis and RD analysis again with the line intensities calculated from several different positions and got similar results with previous analysis with the intensities calculated from the peak position. Thus, we exclude the systematic bias from the choice of positions for measuring the line intensities.

4. DISCUSSION

Though the morphology and kinematics of molecular outflows have been widely studied, there is a lack of studies towards some other physical properties (e.g., the variation of temperature and density with velocity). CO mid-J observations as complements of existed low-J observations are required to constrain the temperature and density of the molecular outflows as a function of velocity, while these mid-J observations are challenging because of atmospheric limits. There are only several studies on the the $T - V$ relation of molecular outflows. A rising CO 3-2/6-5 ratio is observed towards the outflow associated with low-mass YSO HH 46 IRS 1(van Kempen et al. 2009). With the density assumed to be constant, the rising ratios at more extreme velocities correspond to lower kinetic temperatures. In the case of the outflow associated with low-mass protostars NGC 1333 IRAS 4A and IRAS 4B, the CO 3-2/6-5 ratios are remarkably constant with velocity (Yıldız et al. 2012). With the assumption of constant density, the constant ratios indicate constant temperatures. Su et al. (2012) have imaged the extremely high velocity

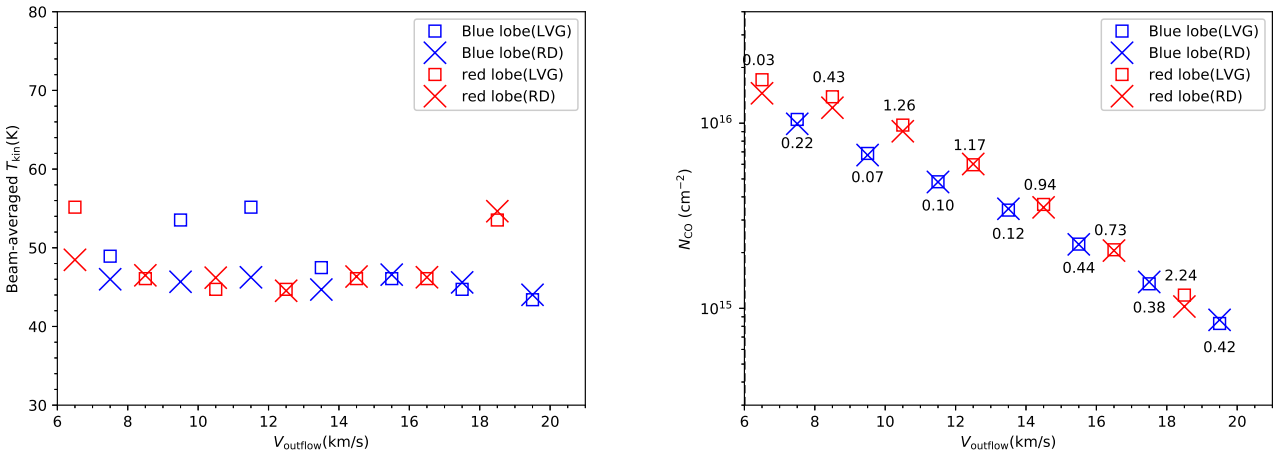

(a) (b)

Figure 4. T-V and N-V diagrams of the G240 outflow, estimated from LVG analysis (blue open squares for blue lobe and red open squares for red lobe) and RD analysis (blue x marker for blue lobe and red x marker for red lobe). The χ^2 calculated from the LVG analysis are shown in the N-V diagram.

(EHV) outflow in CO (2-1) and CO (3-2) associated with the high-mass YSO G5.89-0.39. With the assumption of a canonical CO fractional abundance of 10^{-4}, an increasing trend of temperature with outflow velocity is found by performing a LVG analysis. Using the CO (6-5), (7-6) and (16-15) lines, Leurini et al. (2015) performed a RD analysis towards the G5.89-0.39 outflow and found a decreasing trend of temperature with increasing velocities. This disagreement seen in results of Su et al. (2012) and Leurini et al. (2015) could be due to different angular resolutions ($3''.4$ compared to $14''.5$) and different energy range ($\Delta E_u \sim 17$K compared to $\Delta E_u \sim 600$K). The different $T-V$ relations found in different outflows and in different angular scales reveal the complexity of molecular outflows. However, with only two or three lines observed, their derived $T-V$ relations must be deduced from fixing other physical parameters, e.g., constant density or constant canonical CO fractional abundance, or from the assumption that the different transitions can be discribed with the same excitation temperature (LTE). To get more proper estimations of the pysical parameters of the molecular outflow, multi-line studies of CO and more sophisticated methods (e.g. LVG) are required.

The LVG analysis and the RD analysis reveal that the G240 outflow is isothermal and has a temperature of $\sim$ 50 K . This value is consistent with temperatures in excess of 50 K probed by van Kempen et al. (2016) for outflows associated with intermediate-mass protostars, and slightly lower than temperatures of outflows associated with low-mass protostars (van Kempen et al. 2009; Yıldız et al. 2012). The isothermal state rules out the jet-driven bow shock models, which predicts temperature rising with outflow velocity and distance, and provides evidence for the wind-driven model (Arce et al. 2007). As molecular cooling dominates the cooling of the shocked material in the outflow at temperatures below 10^4 K (Hollenbach 1997) and the cooling rate increases as n^2, molecular cooling is very efficient for the typical density of a wind-driven outflow. Thus, an isothermal state could be reached in a wind-driven outflow. We noticed that there are faint bow-shaped H_2 features near the YSO IRAS 07427-2400, suggesting that the jet-driven outflows may also exist. However, as the average T-V relation of the outflowing gas agrees with the wind-driven model and the kinematics and morphology of the molecular outflow can also be qualitatively interpreted by the wide-angle wind-driven model (Qiu et al. 2009), we conclude that even if the jet-driven outflows and the wind-driven outflows were coexisting in the G240 outflow, the wide-angle wind entrainment plays a more important role in driving the G240 outflow. It should be noted that, most existing outflow models have parameters typical of outflows driven by low-mass YSOs. It is necessary to compare the observational results of outflows driven by high-mass YSOs with models of similar physical conditions. Statics of outflows associated with high-mass star-forming regions are also essential for us to better understand the driven mechanism of massive outflows and the forming process of high-mass stars.

The LVG analysis reveals that the lower limits of gas densities are $\sim 10^5$ cm^{-3} at the velocities where

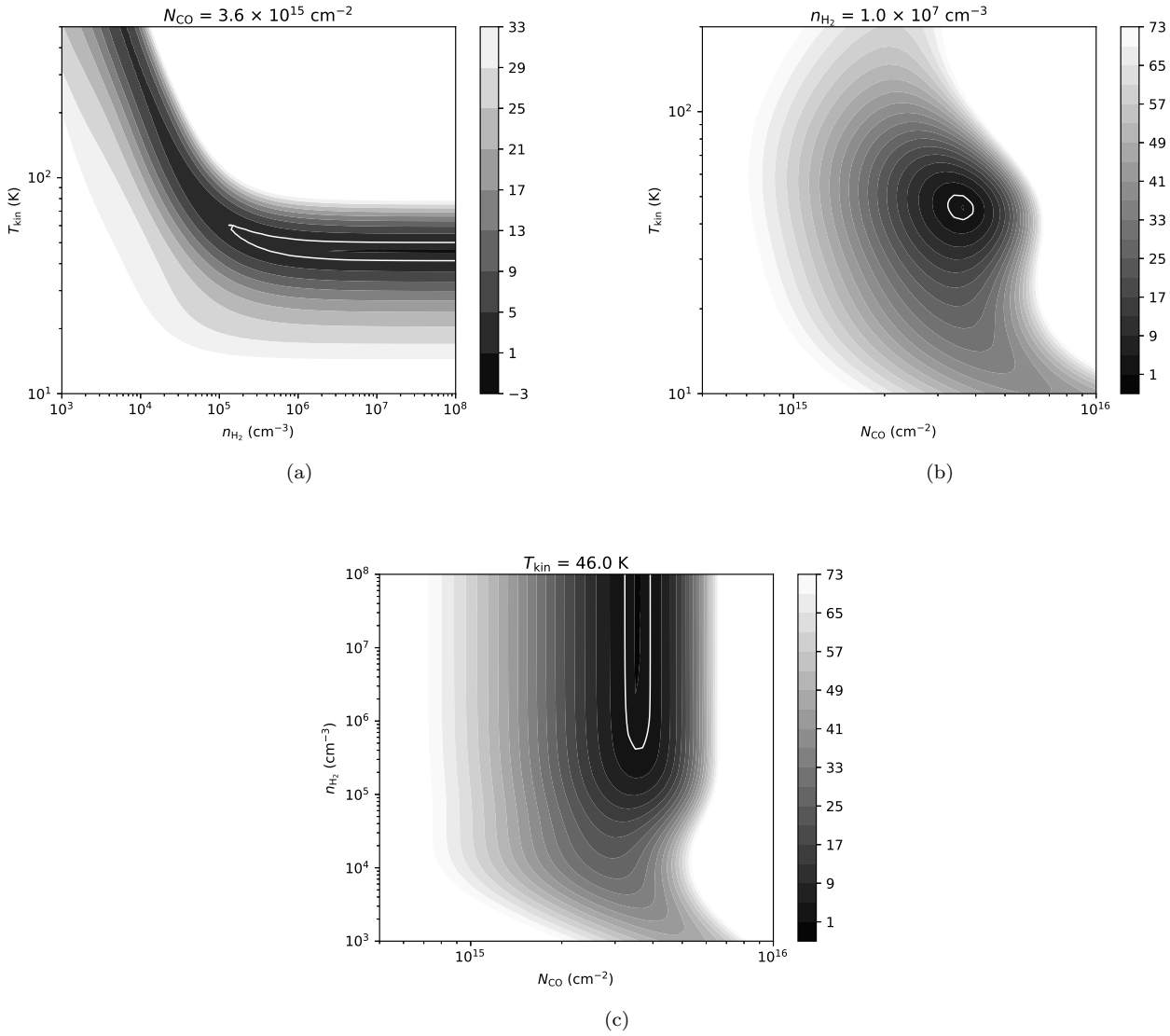

Figure 5. The χ^2 distribution for G240 outflow at 82 km s^{-1} in the (a) [T, n], (b) [T, N], (c) [n, N] planes, with all other parameters fixed to the parameters of the best fitting results at this velocity. The $\chi^2_{\rm red}$ of the best fitting result is ∼0.94 at 82 km s^{-1}. The Solid contours show the 1σ confidence levels.

$\chi^2_{\rm red} \sim 1$. We have found a decreasing trend of the beam averaged CO column density with gas velocity. As shown in the N-V diagram of Figure 4, for each velocity bin (2 km s^{-1}), the beam averaged CO column density drops from $\sim 2 \times 10^{16}$ cm^{-2} to $\sim 8 \times 10^{14}$ cm^{-2} within 15 km s^{-1}. In the optically thin case, the beam averaged CO column density could be related to gas density $n_{\rm H_2}$ through the expression:

$$N_{\rm CO} = n_{\rm H_2} \times \Delta V \times \frac{1}{dv/dr} \times X_{\rm CO} \times f_{\rm b}, \qquad (2)$$

where $f_{\rm b}$ is the beam filling factor, $X_{\rm CO}$ the CO/H$_2$ abundance ratio, ΔV the velocity interval and dv/dr is the velocity gradient. A drop in $N_{\rm CO}$ at more extreme velocities indicates the decrease of one or serveral of these parameters. To explore how the effect of beam dilution influence our results, we vary the beam filling factors from 0.2 to 1 and then perform the LVG analysis again. We find that modelling with different beam filling factors mainly affect the N-V diagram, with minor change in the T-V diagram and density limits. This could be resulted from the degeneracies of the beam filling factor with CO column density in the optically thin case.

As shown in Figure 3 of Qiu et al. (2009), the source size are $\sim 20''$ and $\sim 10''$ at the velocities of $\sim \pm$ 6 km s^{-1} and $\sim \pm$ 20 km s^{-1} with respect to the cloud velocity, corresponding to beam filling factors of $\sim$ 0.5

and ~ 0.2, respectively. Considering the 2.5 times drop in the beam filling factor, the 25 times drop in the beam averaged CO column density indicates ~ 10 times decrease in the CO column density. Due to the lack of other informations, we cannot assess whether the CO abundance ratio or the velocity gradient has attributed to the drop of CO column density at high velocities. As shown in Arce et al. (2007), the wind-driven models predict that the wind density decreases with velocity and distance from the driving source. Thus, if we assume the CO abundance ratio and the velocity gradient to be constant, the decrease of CO column density could be interpreted by a decrease of gas density with velocity.

5. SUMMARY

We have presented a CO multi-transition (CO 2-1, 3-2, 6-5, 7-6) study towards the molecular outflow of the high-mass star-forming region G240. The morphologies seen in four lines are very similar. With the LVG analysis, we have constrained the temperatures to ~ 50 K and found a decreasing trend of CO column density with gas velocity. We also constrain the H_2 density to values higher than $n \sim 10^5$ cm^{-3} and found that the outflowing gas is thermalized. With the RD analysis, we found similar results in the temperature and the CO column density. The T-V relation of the G240 outflow agrees well with the wide-angle wind-driven model. Assuming a constant CO abundance ratio and a constant velocity gradient, we detect a decreasing gas density with velocity, which is also consistent with the wide-angle wind-driven model.

REFERENCES

Andrae, R., Schulze-Hartung, T., & Melchior, P. 2010, arXiv:1012.3754

Arce, H. G., Shepherd, D., Gueth, F., et al. 2007, Protostars and Planets V, 245

Arce, H. G., Mardones, D., Corder, S. A., et al. 2013, ApJ, 774, 39

Bachiller, R. 1996, ARA&A, 34, 111

Banerjee, R., & Pudritz, R. E. 2006, ApJ, 641, 949

Beuther, H., Schilke, P., Sridharan, T. K., et al. 2002, A&A, 383, 892

Beuther, H., Schilke, P., Gueth, F., et al. 2002, A&A, 387, 931

Caratti o Garatti, A., Froebrich, D., Eislöffel, J., Giannini, T., & Nisini, B. 2008, A&A, 485, 137

Caswell, J. L. 1997, MNRAS, 289, 203

Caswell, J. L. 2003, MNRAS, 341, 551

Chen, H.-R., Su, Y.-N., Liu, S.-Y., et al. 2007, ApJL, 654, L87

Ferreira, J., Dougados, C., & Cabrit, S. 2006, A&A, 453, 785

Frank, A., Ray, T. P., Cabrit, S., et al. 2014, Protostars and Planets VI, 451

Fukui, Y., Iwata, T., Mizuno, A., Bally, J., & Lane, A. P. 1993, Protostars and Planets III, 603

Goldsmith, P. F., & Langer, W. D. 1999, ApJ, 517, 209

Gueth, F., & Guilloteau, S. 1999, A&A, 343, 571

Hatchell, J., Fuller, G. A., & Ladd, E. F. 1999, A&A, 344, 687

Hollenbach, D. 1997, Herbig-Haro Flows and the Birth of Stars, 182, 181

Hughes, V. A., & MacLeod, G. C. 1993, AJ, 105, 1495

Hunter, T. R. 1997, Ph.D. Thesis, 238

Kumar, M. S. N., Bachiller, R., & Davis, C. J. 2002, ApJ, 576, 313

Kumar, M. S. N., Fernandes, A. J. L., Hunter, T. R., Davis, C. J., & Kurtz, S. 2003, A&A, 412, 175

Lada, C. J. 1985, ARA&A, 23, 267

Lee, C.-F., Mundy, L. G., Reipurth, B., Ostriker, E. C., & Stone, J. M. 2000, ApJ, 542, 925

Lee, C.-F., Stone, J. M., Ostriker, E. C., & Mundy, L. G. 2001, ApJ, 557, 429

Lee, C.-F., Mundy, L. G., Stone, J. M., & Ostriker, E. C. 2002, ApJ, 576, 294

Lee, C.-F., Hirano, N., Zhang, Q., et al. 2015, ApJ, 805, 186

Leurini, S., Wyrowski, F., Wiesemeyer, H., et al. 2015, A&A, 584, A70

Li, Z.-Y., & Shu, F. H. 1996, ApJ, 472, 211

Machida, M. N., Inutsuka, S.-i., & Matsumoto, T. 2008, ApJ, 676, 1088-1108

Machida, M. N. 2017, arXiv:1711.00384

MacLeod, G. C., Scalise, E., Jr., Saedt, S., Galt, J. A., & Gaylard, M. J. 1998, AJ, 116, 1897

Masson, C. R., & Chernin, L. M. 1993, ApJ, 414, 230

Maud, L. T., Moore, T. J. T., Lumsden, S. L., et al. 2015, MNRAS, 453, 645

McCutcheon, W. H., Sato, T., Dewdney, P. E., & Purton, C. R. 1991, AJ, 101, 1435

Migenes, V., Horiuchi, S., Slysh, V. I., et al. 1999, ApJS, 123, 487

Pudritz, R. E., Rogers, C. S., & Ouyed, R. 2006, MNRAS, 365, 1131

Pudritz, R. E., Ouyed, R., Fendt, C., & Brandenburg, A. 2007, Protostars and Planets V, 277

Qiu, K., Zhang, Q., Wu, J., & Chen, H.-R. 2009, ApJ, 696, 66

Qiu, K., Zhang, Q., Menten, K. M., et al. 2014, ApJL, 794, L18

Raga, A., & Cabrit, S. 1993, A&A, 278, 267

Ren, J. Z., Liu, T., Wu, Y., & Li, L. 2011, MNRAS, 415, L49

Sakai, N., Nakanishi, H., Matsuo, M., et al. 2015, PASJ, 67, 69

Santiago-García, J., Tafalla, M., Johnstone, D., & Bachiller, R. 2009, A&A, 495, 169

Shang, H., Allen, A., Li, Z.-Y., et al. 2006, ApJ, 649, 845

Shepherd, D. S., & Churchwell, E. 1996, ApJ, 457, 267

Shepherd, D. S., Watson, A. M., Sargent, A. I., & Churchwell, E. 1998, ApJ, 507, 861

Shu, F. H., Adams, F. C., & Lizano, S. 1987, ARA&A, 25, 23

Shu, F. H., Najita, J., Ostriker, E. C., & Shang, H. 1995, ApJL, 455, L155

Shu, F. H., Ruden, S. P., Lada, C. J., & Lizano, S. 1991, ApJL, 370, L31

Su, Y.-N., Zhang, Q., & Lim, J. 2004, ApJ, 604, 258

Su, Y.-N., Liu, S.-Y., Chen, H.-R., & Tang, Y.-W. 2012, ApJL, 744, L26

Trinidad, M. A. 2011, AJ, 142, 147

van der Tak, F. F. S., Black, J. H., Schöier, F. L., Jansen, D. J., & van Dishoeck, E. F. 2007, A&A, 468, 627

van Kempen, T. A., van Dishoeck, E. F., Güsten, R., et al. 2009, A&A, 501, 633

van Kempen, T. A., Hogerheijde, M. R., van Dishoeck, E. F., et al. 2016, A&A, 587, A17

Wu, Y., Wei, Y., Zhao, M., et al. 2004, A&A, 426, 503

Wu, Y., Zhang, Q., Chen, H., et al. 2005, AJ, 129, 330

Yeh, S. C. C., Hirano, N., Bourke, T. L., et al. 2008, ApJ, 675, 454-463

Yıldız, U. A., Kristensen, L. E., van Dishoeck, E. F., et al. 2012, A&A, 542, A86

Zhang, Q., Ho, P. T. P., Wright, M. C. H., & Wilner, D. J. 1995, ApJL, 451, L71

Zhang, Q., Hunter, T. R., Brand, J., et al. 2001, ApJL, 552, L167

Zhang, Y., Arce, H. G., Mardones, D., et al. 2016, ApJ, 832, 158